

Robust Cylindrical Plasmonic Nano-Antennas for Light-Matter Interaction

Kaushal Choonee* and Richard R. A. Syms

Abstract—A cylindrical metallic plasmonic nano-antenna consisting of a shell supporting a disk, named capped shell, is proposed and studied by frequency domain finite element analysis. This new topology is shown to be weakly dependent on the radius of the structure and is therefore suitable for fabrication by parallel processes such as island lithography which generates a pseudo-random array with a distribution of diameters. Furthermore, compared to similar resonators such as rods, disks and shells, the capped shell generates a larger volume with high fields, and is hence useful as a nano-antenna for light-matter interaction.

1. INTRODUCTION

Optical antennas have received considerable attention recently due to their ability to confine electromagnetic energy and influence light matter interactions on the nano-scale [1, 2]. They are typically fabricated by serial processes such as electron beam lithography (EBL) and focussed ion beam (FIB) machining [3] but patterning techniques that trade precision for speed and parallelism remain popular. Two such techniques are nanosphere [4] and island lithography [5] which are particularly suitable for generating arrays of cylindrical nanostructures. In this paper, cylindrical plasmonic resonators that can be fabricated with these parallel methods are numerically investigated. Four geometries are considered, namely; rods, shells, disks, and capped shells — which consist of a shell supporting a disk.

Island lithography (ISL) and nanosphere lithography (NSL) are well established techniques that can be combined with a vertical etching process to form disordered or ordered arrays of nanopillars (see, e.g., [5–7]). Further metallization and ion etching steps can be performed to enable the fabrication of plasmonic antennas and a possible parallel fabrication scheme is illustrated in Fig. 1. The starting point is a mask defined by ISL or a similar process. Using this mask, a cylindrical pillar is formed by a vertical etching process, such as reactive ion etching. The pillar is conformally coated and then exposed to an ion beam that preferentially etches the corners of the metalised pillar, as described in [8]. The resulting structure is termed capped shell. Alternatively, the horizontal facing layer can be completely removed with a sputter etching process to leave a metallic shell (known as sidewall transfer). With the proposed fabrication process, the antenna height is determined by the reactive ion etching process whilst the diameter is set by ISL.

In this study, cylindrical plasmonic resonators that can be fabricated using the scheme described in Fig. 1 are considered. Such tubular plasmonic structures have been used, e.g., as high performance biosensors (see, e.g., [9]) or as field concentrators for trapping of nanoparticles [10]. We restrict our discussion to isolated structures rather than arrays and also focus on fabrication methods such as ISL, which generate a distribution of diameters rather than a single size. The lack of control over the diameter is normally a limiting factor in the design of nano-antennas, but it is shown that the shell and a novel geometry termed capped shell are relatively insensitive to changes in radius. Furthermore, we consider

Received 9 May 2014, Accepted 10 June 2014, Scheduled 24 July 2014

* Corresponding author: Kaushal Choonee (kaushal.choonee@imperial.ac.uk).

The authors are with the Optical and Semiconductor Devices Group, EEE Department, Imperial College London, Exhibition Road, London SW7 2AZ, UK.

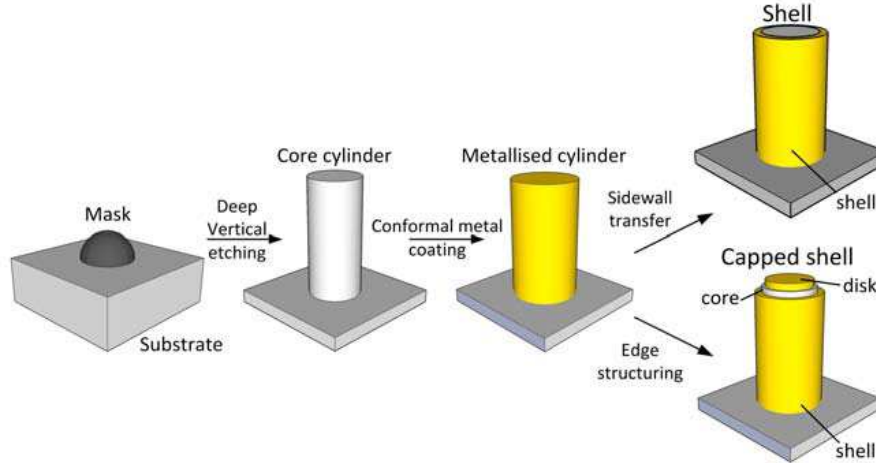


Figure 1. Illustration of a fabrication process suitable for generating the cylindrical structures. The starting point is a mask defined by island lithography, which determines the radius of the nano-resonator.

applications in the area of field matter interactions such as enhanced fluorescence [11], where a large region of interaction is favoured over an extremely confined field, and we show that the proposed capped shell resonator is particularly suitable.

The behaviour of the capped shell can be understood from the behaviour of its constituent elements namely rods, disks, and shells, and, in Section 2, these are first investigated separately by 2D finite element analysis (FEA) and then combined together into the capped shell. In Section 3, 3D simulations are carried out to verify the behaviour. Conclusions are presented in Section 4.

2. ANTENNA DESIGN AND SIMULATION

2.1. Simulation Parameters

Simulations were carried out using a full wave frequency domain FEA solver (Comsol Multiphysics [12]) with an excitation wavelength of $\lambda_0 = 633$ nm. A 2D cylindrical geometry (ρ, ϕ, z) is adopted where the geometry is assumed to be invariant along ϕ . The geometry consists the antenna surrounded by a dielectric medium of refractive index $n_s (= \sqrt{\epsilon_s})$.

A TM_0 incident wave (with the magnetic field having only an azimuthal component, H_ϕ) is used to excite the structure and resonances are monitored by computing the extinction cross section (σ_{ext}) with different geometrical parameters. The extinction cross section is the sum of the scattering (σ_{scatt}) and absorption (σ_{abs}) cross sections. The scattering cross section is defined as: $\sigma_{\text{scatt}} = (1/I_0) \times \iint S_{\text{sc}} dS$, where S_{sc} is the Poynting vector of the scattered field oriented normally to the outer surface, S , of the particle, and I_0 is the incident wave intensity. The absorption cross section is defined as: $\sigma_{\text{abs}} = (1/I_0) \times \iiint Q dV$, where Q is the power loss density in the particle of volume, V . For meaningful comparison of different geometries, a normalised extinction cross section $\sigma_{\text{norm}} = \sigma_{\text{ext}}/S$ is used. In addition to σ_{norm} , the maximum field enhancement, $|E_{\text{max}}/E_0|$, in the near field of the scatterer is also monitored as function of the geometrical parameters. $|E_{\text{max}}/E_0|$ is found by scanning the region surrounding the metallic nanostructure for the maximum value of $|E/E_0|$.

Furthermore, a parameter termed interaction volume, V_C , is introduced. V_C is the volume in the superstrate outside the volume occupied by the resonator over which the field enhancement $|E/E_0|$ is greater than $|E_C/E_0|$. $|E_C/E_0|$ is the minimum field enhancement considered useful. In nano-photonics, energy confinement is normally measured in terms of an effective mode volume [13], which accounts for the energy confined within the entire resonator. In applications where the amplified electric field is used to interact with matter, such as enhanced fluorescence or harmonic generation, V_C provides a measure of the number of particles exposed to high fields and is a more suitable figure of merit. In this work, an arbitrary field amplification of $|E_C/E_0| \geq 10$ is assumed to define the volume of interest. The relevant

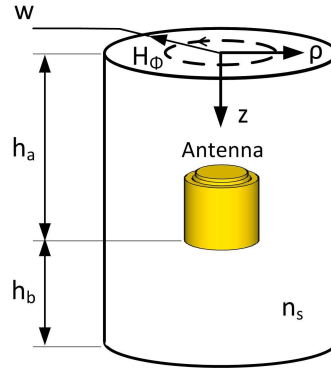


Figure 2. Illustration of the computational domain with the key dimensions labelled. PMLs (not shown) of thickness 150 nm surround the domain.

value of $|E_C/E_0|$ to use will depend on the application.

The computational domain is bound by perfectly matched layers (PMLs) to absorb the scattered waves and the computational size is $w = 1000$ nm in the ρ direction and $h_a = 1250$ nm and $h_b = 1250$ nm in the z axis. The cell geometry (excluding the PML of thickness 150 nm) and the antenna with its key dimensions are illustrated in Fig. 2. The corners of the metal are rounded by 2.5 nm to improve convergence.

The dielectric constant of the metal is calculated from the Drude model such that $\epsilon_{rm} = \epsilon_{r\infty} - \omega_p^2/(\omega - j\omega_\tau)$. Here, $\epsilon_{r\infty}$ is the high frequency dielectric constant, ω_p is the plasma frequency of the electron cloud, ω is the excitation frequency, and ω_τ is the damping frequency. From [14] $\epsilon_{r\infty} = 9.07$, $\omega_p = 13.5 \times 10^{15}$ rads $^{-1}$, $\omega_\tau = 0.115 \times 10^{15}$ rads $^{-1}$ for Au, giving $\epsilon_{rm} = -11.47 - 0.79j$ at $\lambda_0 = 633$ nm. The refractive index of the surrounding medium is set to unity ($n_s = 1$), which effectively represents the case where the substrate and superstrate are matched. For the shell and capped shell geometries, the refractive index of the core is also equal to n_s .

To understand the behaviour and evaluate the performance of the capped shell resonator, the fundamental building blocks are first studied separately. In Section 2.2, the rod antenna is examined, followed by a study of the circular disk and shell resonators in Section 2.3 and Section 2.4. In Section 2.5, the capped shell geometry is considered.

2.2. Rod

Nano-scale metallic rods have been investigated as waveguides for confined one dimensional beams [15, 16] and as half-wave antennas [17]. Assuming cylindrical symmetry as in [15] the fundamental mode corresponds to a so called transverse magnetic mode (TM₀) with the \underline{H} field having only a component in ϕ , H_ϕ , and the wave propagating along z with propagation constant β_Z , which is a function of radius r . The antenna resonates whenever $\beta_Z \times L \approx \nu\pi$, where ν is an integer denoting the mode number (see, e.g., [1]). The approximation is due to the fact that the additional phase picked up on reflection from the ends of the cylinder (see [17]) is neglected.

The resonant behaviour of such metallic rods is verified by computing the maximum field enhancement $|E_{\max}/E_0|$ and σ_{norm} for a range of radii (r) and lengths (L) and the results are plotted as colour maps in Fig. 3(b) and Fig. 3(c). The simulation parameters described in Section 2.1 are used. For small radii, strong resonances are obtained, whilst for $r > 50$ nm, the resonances are noticeably weaker. This is consistent with the results of [15, 16] where the wave becomes less confined to the metal at larger radii. Intuitively, by analogy with a lightning rod, this is expected as sharper features are better field attractors. In addition, two distinct bands are observed as L is increased and these correspond to the $\nu = 1$ and $\nu = 2$ resonant lengths. For example, at $r = 18$ nm, the first resonant length is $L = 87.5$ nm whilst the second resonant length is $L = 237.5$ nm. The difference in lengths indicates that the effective wavelength of the standing wave is ≈ 300 nm, which is comparable to the results of [17] for Au rods. The interaction volume, V_C , normalised to its maximum value is qualitatively illustrated as a function

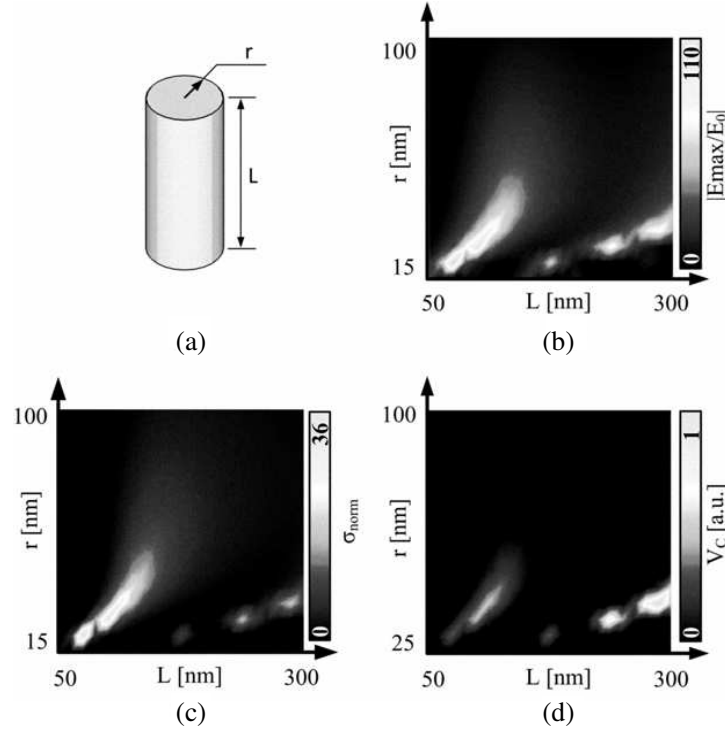


Figure 3. (a) Illustration of the rod geometry, colour maps showing resonant behaviours as a function of r and L in terms of (b) $|E_{\max}/E_0|$ and (c) σ_{norm} . (d) Qualitative map of the interaction volume, V_C , with varying geometry.

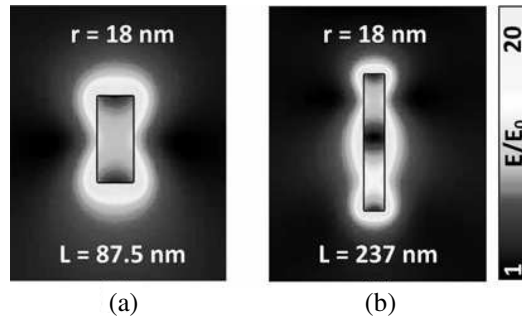


Figure 4. $|E/E_0|$ field map for (a) $r = 18$ nm, $L = 87.5$ nm and (b) $r = 18$ nm, $L = 237$ nm.

of L and r in Fig. 3(d). The latter indicates that the second resonance band, with larger L , provides a larger interaction volume than the first band even if the extinction is smaller.

Normalised electric field maps $|E/E_0|$ showing the field hot spots at the ends of the metallic rods on resonance are shown for $r = 18$ nm and $L = 97.5$ nm, and for $r = 18$ nm and $L = 237.5$ nm, in Fig. 4(a) and (b) respectively. The field maps show that the large resonator exhibits a larger area of high field and hence confirms why V_C is larger in this range.

2.3. Disk

The disk or circular patch can be considered as a limiting case of a short rod and supports radially propagating SPP known as Hankel-type SPPs [18]. The dispersion relation in this case is the same as that of an insulator metal insulator (IMI) slab waveguide in a planar geometry.

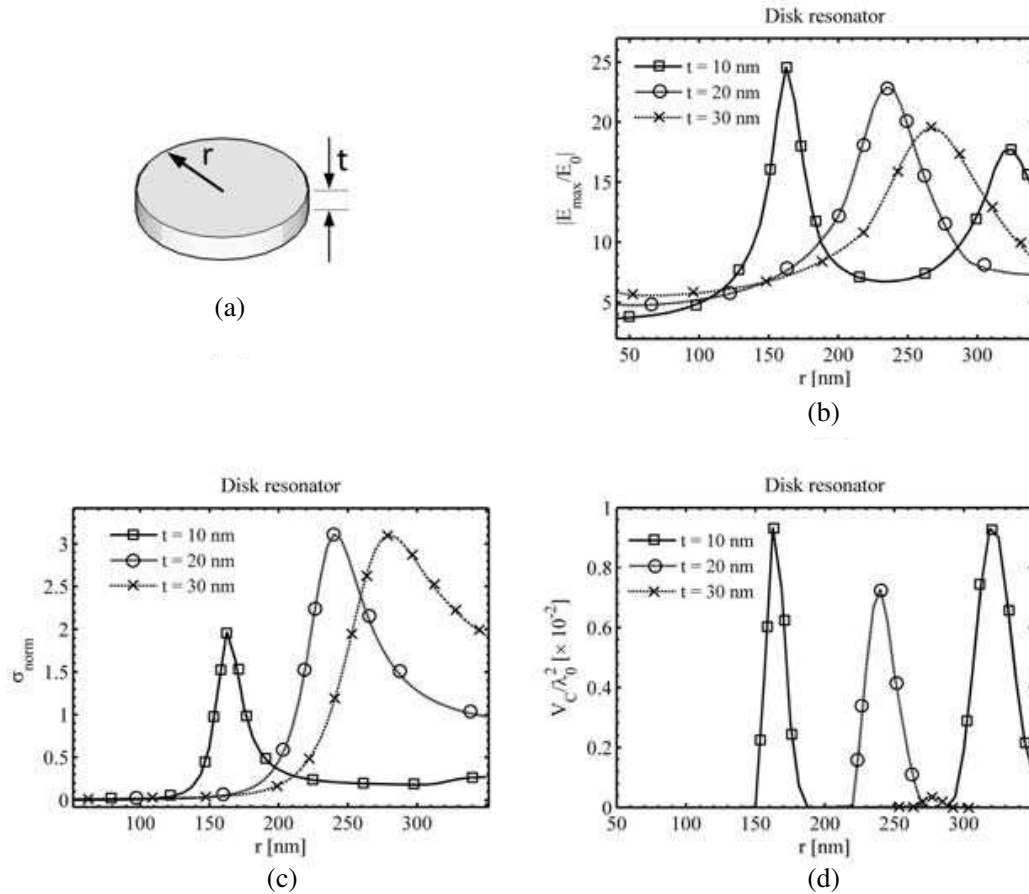


Figure 5. (a) Illustration of the metallic disk. Resonance of the disk at different thicknesses as a function of r in terms of (b) $|E_{\max}/E_0|$, and (c) σ_{norm} . (d) Normalised interaction volume, V_C/λ_0^2 , as a function of r for disks of different thicknesses.

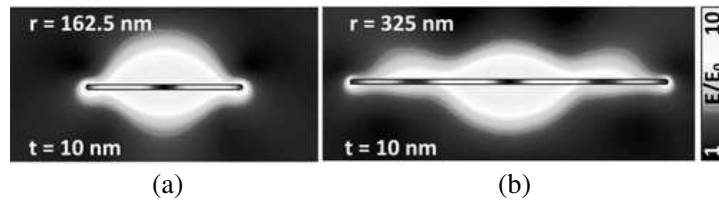


Figure 6. Colour map of $|E/E_0|$ for (a) $r = 162.5$ nm and (b) $r = 325$ nm. The colour scale is restricted to 10 for clarity.

The geometry of the disk antenna of thickness t and radius r is illustrated in Fig. 5(a). The resonances are computed by FEA using the parameters described in Section 2.1 and are illustrated in Fig. 5(b) and Fig. 5(c) as a function of radius at different thicknesses. For $t = 10$ nm, clear resonances are observed at $r = 162.5$ nm and $r = 325$ nm, corresponding to the first and second order modes respectively. For larger values of t , σ_{norm} increases and this is attributed to a larger absorption (σ_{abs}). As shown in Fig. 5(d), V_C is zero except for a ≈ 50 nm band centred on the resonant radii for $t = 10$ nm and $t = 20$ nm. For the 30 nm thick disk, hardly any useful interaction volume is generated. The E -field distribution at resonance is illustrated in Figs. 6(a) and (b) and only moderate field enhancements ($|E/E_0| \sim 10$) are obtained at the edges.

2.4. Shell

The behaviour of cylindrical metallic shell structures has been studied analytically and numerically [16, 19]. In particular, Novotny and Hafner [16] present findings for a circular dielectric waveguide with a finite metal cladding and show that a number of hybrid modes (EH and HE) can be supported in addition to the TM_0 mode. Therefore, the excitation method used and the 2D simulation may not accurately capture the behaviour of the shell antenna due to the imposed symmetry. However, the 2D approximation still yields useful information and the results are presented below.

The simulation parameters described in Section 2.1 are used and the inner radius (r) of the shell and its length (L) are varied whilst keeping the shell thickness constant at $t = 10$ nm (see Fig. 7(a)). The peak field enhancement $|E_{\max}/E_0|$ and the normalised cross section σ_{norm} are computed and illustrated as colour maps in Figs. 7 (b) and (c) respectively. Two distinct bands are observed at $L \approx 100$ nm and $L \approx 250$ nm, and these correspond to first and second order plasmonic Fabry-Perot resonances.

For large radii, $r > 30$ nm, the resonance bands are vertical indicating that the guided mode is insensitive to the radius of the shell, which is consistent with the results presented in [16] for the TM mode. The field distributions in this case are illustrated in Figs. 8(a) and (b) for $r = 62.5$ nm and $L = 125$ nm and $L = 250$ nm highlighting the fact that the field is closely bound to the shell. As r is increased beyond 50 nm, σ_{norm} is essentially unchanged whilst $|E_{\max}/E_0|$ drops but remains of the order of ~ 25 . In terms of interaction volume, as illustrated in Fig. 7(d), a larger useful volume is obtained on the second band ($L = 250$ nm), although the extinction and peak fields are larger on the first band.

For small radii, $r < 30$ nm, the resonance condition is more strongly dependent on r as the E -fields from opposite sides of the shell extend far enough to interact. This is illustrated in the E -field maps for small radii in each resonant band in Figs. 8(c) and (d). Intuitively, the behaviour of the shell converges to that of the rod at small radii, and larger field enhancements (~ 70) are obtained in this regime.

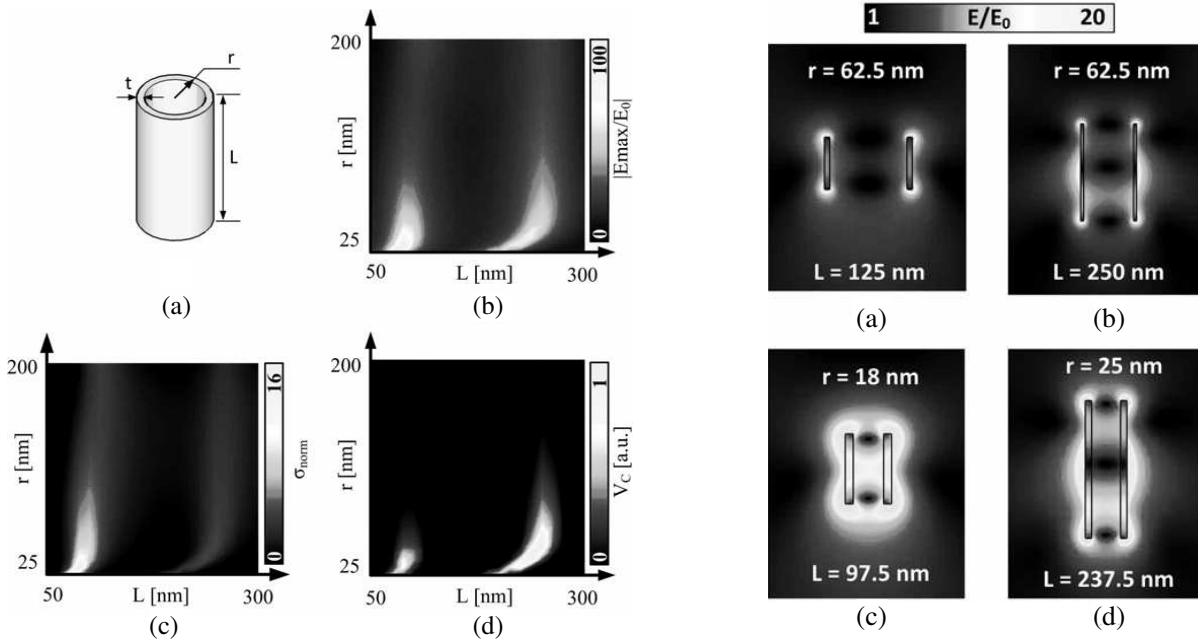


Figure 7. (a) Illustration of the shell geometry. Colour maps showing resonant behaviours as a function of r and L in terms of (b) $|E_{\max}/E_0|$, (c) σ_{norm} , and (d) V_C .

Figure 8. E -field maps of the shell resonator at (a) $r = 62.5$ nm, $L = 125$ nm, (b) $r = 62.5$ nm, $L = 250$ nm, (c) $r = 18$ nm, $L = 97.5$ nm, and (d) $r = 25$ nm, $L = 237.5$ nm. Note, the $|E/E_0|$ colour scale is restricted to 20 for clarity.

2.5. Capped Shell

In this section, the disk and shell resonators are combined as illustrated in Fig. 9(a). The gap, g , is set to $t/2$, where $t = 10$ nm. The inner shell radius is related to the disk radius by $r_{\text{shell}} = r + g/2$, and both the antenna radius (r) and length (L) are varied and the peak field enhancement $|E_{\text{max}}/E_0|$, the normalised cross section σ_{norm} and interaction volume V_C are monitored, using the parameters described in Section 2.1. By analogy to [20] where small gaps are formed in dolmen structures, the capped shell is expected to generate large field enhancement at the gap. The resonances are illustrated in Figs. 9(b), (c), and (d).

Distinct resonant bands are observed when both the radius and length are varied over the range denoted by the axes. The first band occurs at $L \approx 87.5$ nm between $r = 25$ nm to $r = 118.5$ nm, as illustrated by the $|E/E_0|$ maps in Figs. 10(a) and (b), and a similar behaviour is observed for the second band at $L \approx 250$ nm, as illustrated in Figs. 10(c) and (d). For small radii, the strong extinction and field enhancement is due primarily to the shell. For larger radii, $r > 100$ nm, and especially around $r = 165$ nm, the resonance bands in Figs. 9(b) and (c) curl. In fact, at $r = 165$ nm, when the disk is in tune, there is a small dark region in the loci map because the disk absorbs the incident energy and shields the shell, effectively lowering the overall extinction and field enhancement. This effect is more obvious in the V_C map where V_C falls to zero when the disk is at resonance. With the disk radius chosen such that it is off resonance, i.e., $50 \text{ nm} < r < 125 \text{ nm}$ and $r > 170 \text{ nm}$, the disk confines enough energy to boost the E -field of the shell and the combined structure exhibits stronger extinctions and larger V_C than the shell of the same size. The E -field maps for this configuration is illustrated in Figs. 10(b) and (d) and highlighting the field enhancement and confinement at the gap.

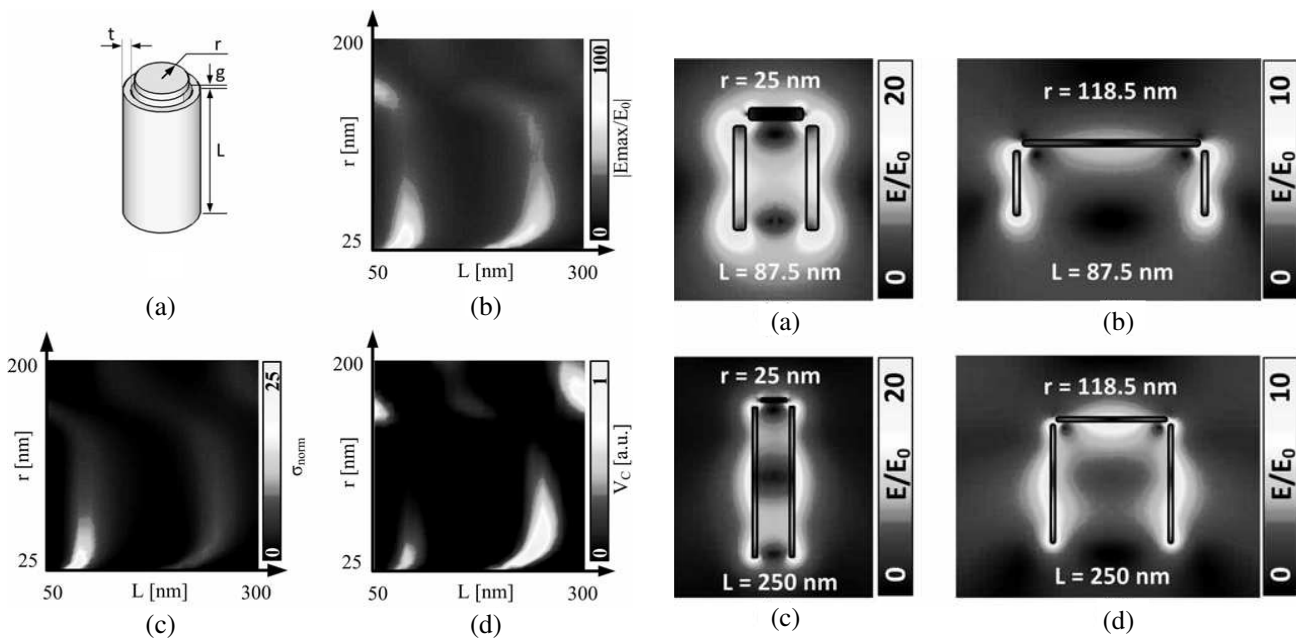


Figure 9. (a) Illustration of the capped shell geometry. Colour maps showing resonant behaviour as a function of r and L in terms of (b) $|E_{\text{max}}/E_0|$, (c) σ_{norm} , and (d) V_C .

Figure 10. E -field maps if the capped shell resonator at (a) $r = 25$ nm, $L = 87.5$ nm, (b) $r = 118.5$ nm, $L = 87.5$ nm, (c) $r = 25$ nm, $L = 250$ nm, and (d) $r = 118.5$ nm, $L = 250$ nm. Note that the $|E/E_0|$ colour scale is restricted as indicated for clarity.

2.6. Discussion: 2D Simulations

In this section, 2D simulation studies of cylindrical structures (invariant along ϕ) have been carried out. The geometries considered include finite rods, thin disks, shells, and shells capped by a thin disk.

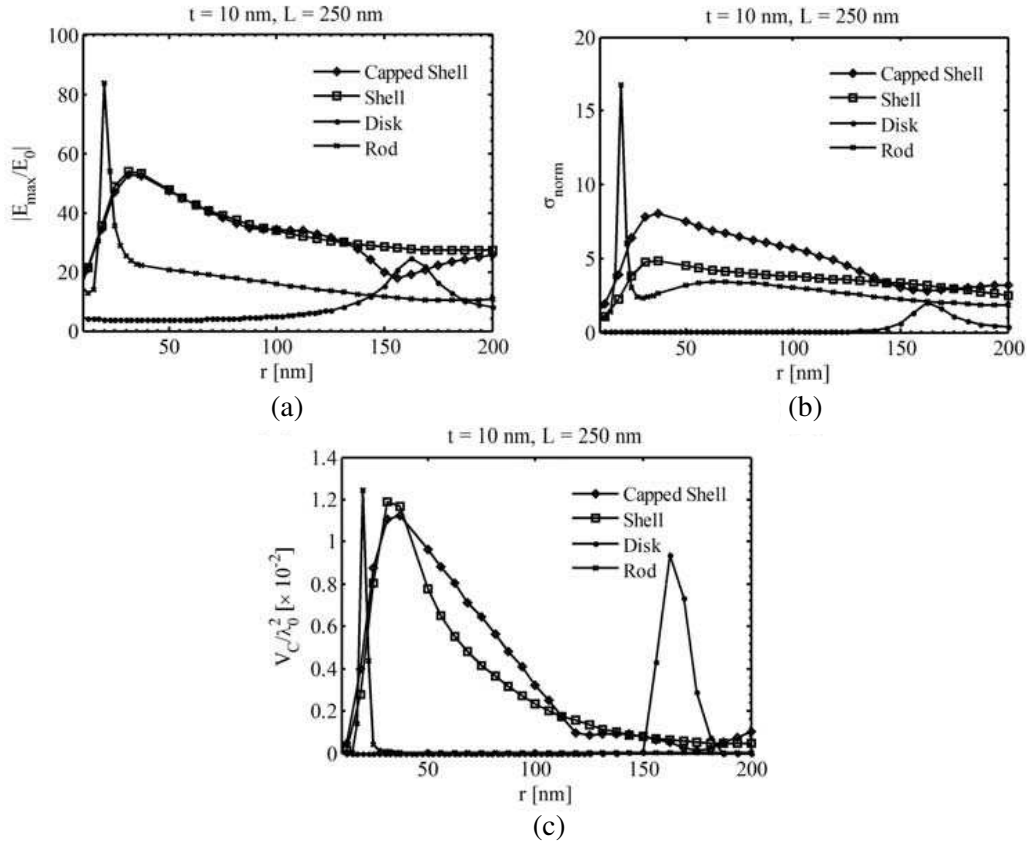


Figure 11. Resonances of the rod, disk, shell, and capped shell structures in terms of (a) $|E_{\max}/E_0|$, (b) σ_{norm} and (c) V_C/λ_0^2 computed in the 2D geometry.

As expected, sharp structures (small r) exhibit high extinction and generate high peak fields. As r is increased, σ_{norm} and $|E_{\max}/E_0|$ drop, as illustrated in Figs. 11(a) and (b) where $|E_{\max}/E_0|$ and σ_{norm} as a function of r at $L = 250$ nm for all four structures are overlaid for comparison. In Fig. 11(c), the associated interaction volume, V_C , is illustrated as a function of r . As indicated by the colour maps in Sections 2.2–2.5, the rod exhibits a narrowband resonance at a small radius, the disk exhibits a weak resonance at $r = 162.5$ nm, whilst the shell, and the capped shell both sustain similar broad resonances whilst maintaining strong peak enhancements and extinctions. Of the four resonators, the capped shell exhibits a useful V_C for a larger range of geometries (see Fig. 11(c)). In the composite structure at $r = 162.5$ nm, when the disk resonates, the overall extinction and field enhancement is lower than that of the shell only because the disk effectively absorbs the incident energy and shields the remainder of the resonator. When the disk is off-resonance, i.e., $r \neq 162.5$ nm, the capped shell exhibits a higher σ_{norm} , a slightly larger V_C/λ_0^2 than the shell and essentially the same peak field enhancement.

As indicated earlier, the 2D formulation limits the computed solutions to symmetric ones when the shell structure in fact supports a variety of modes. Moreover, with the exciting wave being normally incident (z), the field overlap with the radially propagating (ρ) Hankel SPP mode of the disk is low, and hence, the field confinement and enhancement at the gap may not be accurately captured. Full 3D simulations of the resonators are carried out in the next section.

A further aspect which is beyond the scope of this study is the effect of unmatched substrate and superstrate on the response of antennas. A typical configuration is that of an optically dense substrate such as silica ($n \approx 1.5$) with an air superstrate ($n = 1$). This has been investigated in, e.g., [21] and a key finding is the increased mode power leakage from the bound plasmonic mode to the radiating mode in the substrate. This can be intuitively deduced from the fact that the effective index of the guided mode is closer to the refractive index of the substrate. As a result, the interaction volume is likely to

be lower, although the shell and capped resonators will still maintain strong resonances over a broad range of radii.

3. 3D SIMULATION

The 2D cylindrical formulation, due to the imposed axial symmetry, limits the type of modes supported. To confirm the behaviour of the resonator without the symmetry restriction, a full 3D simulation with a plane wave excitation is carried out.

3.1. 3D Simulation Parameters

The computational domain illustrated in Fig. 2 is used with the cylindrical outer edge replaced by a cuboid. For computational efficiency, the domain is shrunk with w set to 500 nm, h_b to 250 nm, and h_a to 800 nm. The same material properties and wavelength as in Section 2.1 are used. The metal thickness (t) is set to 10 nm and the gap (g) is set to 5 nm. The edges of the metal are rounded by 2.5 nm to improve convergence. For all resonators (except the disk) the height, L , is set to 250 nm and the structure is simulated over a range of r . The structure is excited by a plane wave with propagation vector inclined at 45° to the horizontal and magnetic component pointing in the y (out-of-plane) direction.

3.2. 3D Simulation Results

The peak field enhancement, normalised extinction and interaction volume for all four resonators are computed and illustrated in Figs. 12(a), (b), and (c). The resonance curves for all resonators, except for

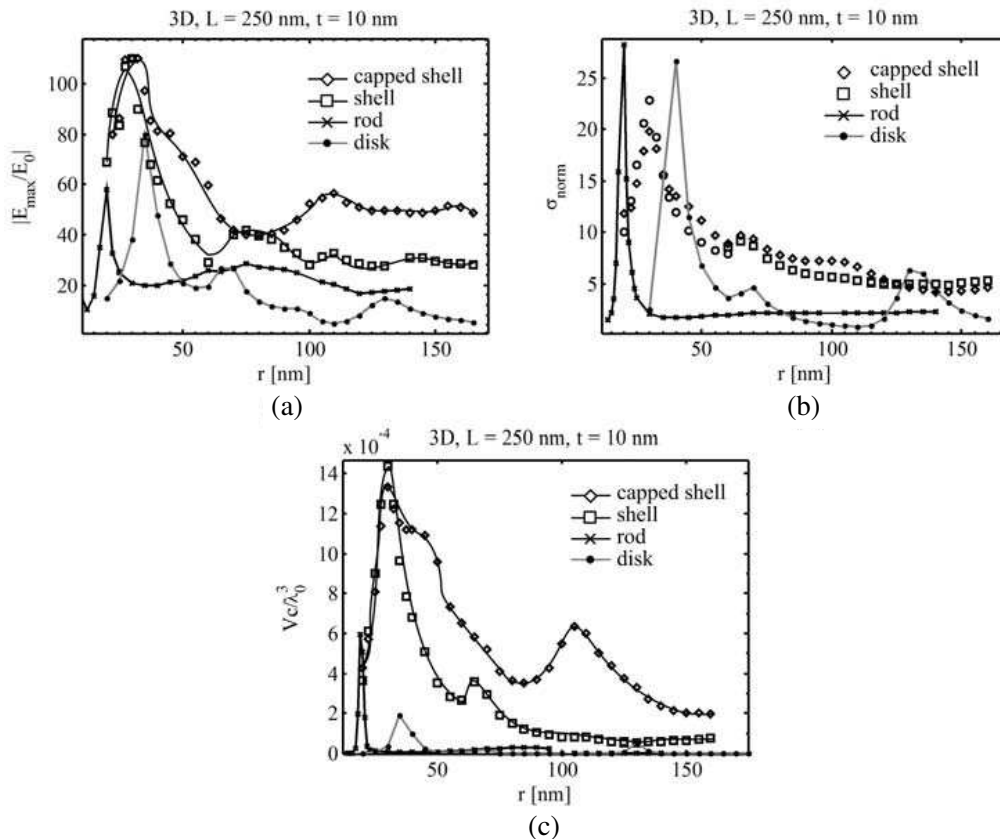


Figure 12. Resonance of capped shell and shell resonator computed using a full 3D model in terms of (a) $|E_{\max}/E_0|$, (b) σ_{norm} , and (c) VC/λ_0^3 . In plot (a) the lines are visual guides, and indicate that the capped shell structure exhibits larger field enhancements than the shell for larger radii.

the disk, broadly follow those of the 2D simulations although σ_{norm} and $|E_{\text{max}}/E_0|$ are higher than in the 2D case, and the capped shell and shell exhibit more pronounced peaks. Furthermore, the capped shell clearly offers a larger V_C than all the resonators because of the field enhancement in the gap.

In the case of the disk, an additional peak is observed at $r = 35$ nm and this is due to a half-wave standing mode across the diameter of the disk. Furthermore, the field enhancements and extinctions in the 3D resonators are significantly larger than in the 2D simulation. The former is because the field discontinuity introduced by the gap is more accurately captured, and the latter because the oblique excitation, with components along the horizontal and vertical directions, interacts more effectively with the resonators. For $r > 100$ nm, the capped shell exhibits slightly stronger field enhancements than the shell, with nearly equal extinctions. The larger peaks field computed in the capped shell for some values of r are attributed to field amplification in the gap. The usefulness and importance of the capped shell is further demonstrated in terms of its interaction volume, V_C , normalised to λ_0^3 , as a function of r in Fig. 12(c). The rod and disk provide a useable interaction volume only over a short range of r ($r = 18$ nm and $r = 35$ nm respectively), whilst the shell and especially the capped shell both provide a larger V_C at resonance and still maintain a significant over the range of radii tested.

4. CONCLUSIONS

In this report, a novel cylindrical plasmonic resonator, termed capped shell, has been proposed and studied by frequency domain FEA at a wavelength of 633 nm. The development of this antenna is driven by the availability of parallel accessible fabrication techniques such as nanosphere or island lithography, combined with edge structuring.

Key advantages of the capped shell are its suitability over a broad range of radii, which makes the structure tolerant to fabrication process variations, as well as its large interaction volume, V_C , relative to similar geometries such as rods, disks, or shells. V_C denotes the accessible volume over which the field amplification is greater than a threshold value and used as a figure of merit to compare the resonators studied. The large V_C of the capped shell, combined with its low sensitivity to the structure radius, makes it a robust platform for field-matter interactions.

The introduction of V_C highlights the trade-off between high field confinement and large interaction volumes, and indicates that traditional parameters such as extinction cross sections may not be the best when designing antennas for field-matter interactions. One such application is metal enhanced fluorescence imaging [10] of molecules at low concentrations where few fluorophores are available per unit volume, and a large interaction volume would be preferred to improve the measured signal.

ACKNOWLEDGMENT

The authors would like to thank Prof. Mino Green for fruitful discussions and valuable input. This work was financially supported by The Leverhulme Trust (F/07 058/BR).

REFERENCES

1. Giannini, V., A. I. Fernández-Domínguez, Y. Sonnefraud, T. Roschuk, R. Fernández-García, and S. A. Maier, "Controlling light localization and light-matter interactions with nanoplasmonics," *Small*, Vol. 6, 2498–2507, 2010.
2. Bharadwaj, P., B. Deutsch, and L. Novotny, "Optical antennas," *Adv. Opt. Photon.*, Vol. 1, 438–483, 2009.
3. Novotny, L. and N. van Hulst, "Antennas for light," *Nature Photon.*, Vol. 5, 83–90, 2011.
4. Chan, G. H., J. Zhao, E. M. Hicks, G. C. Schatz, and R. P. van Duyne, "Plasmonic properties of copper nanoparticles fabricated by nanosphere lithography," *Nano Lett.*, Vol. 7, 1947–1952, 2007.
5. Green, M. and F. M. Liu, "SERS substrates fabricated by island lithography: The silver/pyridine system," *J. Phys. Chem. B*, Vol. 107, 13015–13021, 2003.
6. Haynes, C. L. and R. P. van Duyne, "Nanosphere lithography: A versatile nanofabrication tool for studies of size-dependent nanoparticle optics," *J. Phys. Chem. B*, Vol. 105, 5599–5611, 2001.

7. Cheung, C. L., R. J. Nikolić, C. E. Reinhardt, and T. F. Wang, "Fabrication of nanopillars by nanosphere lithography," *Nanotechnology*, Vol. 17, 1339, 2006.
8. Choonee, K., R. R. A. Syms, and M. Green, "Optical resonators fabricated by nanostructuring at mesa edges," *Micro and Nano Engineering*, London, UK, 2013.
9. McPhilControlling light localization and light-matter interactions with nanoplasmonics," *Small*, Vol. 6, 2498–2507, 2010.
10. Wang, K., E. Schonbrun, P. Steinvurzel, and K. B. Crozier, "Trapping and rotating nanoparticles using a plasmonic nano-tweezer with an integrated heat sink," *Nature Communications*, Vol. 2, 469, 2011.
11. Aslan, K., I. Gryczynski, J. Malicka, E. Matveeva, J. R. Lakowicz, and C. D. Geddes, "Metal-enhanced fluorescence: An emerging tool in biotechnology," *Curr. Opin. Biotechnol.*, Vol. 16, 55–62, 2005.
12. COMSOL Multiphysics, available: <http://www.comsol.com/>.
13. Maier, S. A., "Plasmonic field enhancement and sers in the effective mode volume picture," *Opt. Express*, Vol. 14, 1957–1964, 2006.
14. Ordal, M. A., L. L. Long, R. J. Bell, S. E. Bell, R. R. Bell, J. R. W. Alexander, and C. A. Ward, "Optical properties of the metals Al, Co, Cu, Au, Fe, Pb, Ni, Pd, Pt, Ag, Ti, and W in the infrared and far infrared," *Appl. Opt.*, Vol. 22, 1099–1119, 1983.
15. Takahara, J., S. Yamagishi, H. Taki, A. Morimoto, and T. Kobayashi, "Guiding of a one-dimensional optical beam with nanometer diameter," *Opt. Lett.*, Vol. 22, 475–477, 1997.
16. Novotny, L. and C. Hafner, "Light propagation in a cylindrical waveguide with a complex, metallic, dielectric function," *Phys. Rev. E*, Vol. 50, 4094–4106, 1994.
17. Novotny, L., "Effective wavelength scaling for optical antennas," *Phys. Rev. Lett.*, Vol. 98, 266802, 2007.
18. Filter, R., J. Qi, C. Rockstuhl, and F. Lederer, "Circular optical nanoantennas: An analytical theory," *Phys. Rev. B*, Vol. 85, 125429, 2012.
19. Al-Bader, S. and M. Imtaar, "Azimuthally uniform surface-plasma modes in thin metallic cylindrical shells," *IEEE J. Quant. Electron.*, Vol. 28, 525–533, 1992.
20. Choonee, K. and R. R. A. Syms, "Folded dipole plasmonic resonators," *Opt. Express*, Vol. 21, 25841, 2013.
21. Veronis, G. and F. Shanhui, "Modes of subwavelength plasmonic slot waveguides," *J. Lightwave Technol.*, Vol. 25, 2511–2521, 2007. lips, J., A. Murphy, M. P. Jonsson, W. R. Hendren, R. Atkinson, F. Hook, A. V. Zayats, and R. J. Pollard, "High-performance biosensing using arrays of plasmonic nanotubes," *ACS Nano*, Vol. 4, 2210–2216, 2010.